Infrared spectroscopy of astrophysically relevant hydrocarbons

Doney, K.D.

8

ASTRONOMICAL INFRARED SPECTRUM OF DEUTERATED POLYCYCLIC AROMATIC HYDROCARBONS

The amount of deuterium locked up in polycyclic aromatic hydrocarbons (PAHs) has to date been an uncertain value. We present a near-infrared (NIR) spectroscopic survey of HII regions in the Milky Way, Large Magellanic Cloud (LMC), and Small Magellanic Cloud (SMC) obtained with AKARI, which aims to search for features indicative of deuterated PAHs (PAD or D_n-PAH) to better constrain the D/H ratio of PAHs. Fifty-three HII regions were observed in the NIR (2.5 - 5 μm), using the Infrared Camera (IRC) on board the AKARI satellite. Through comparison of the observed spectra with a theoretical model of deuterated PAH vibrational modes, the aromatic and (a)symmetric aliphatic C-D stretch modes were identified. We see emission features between 4.4 - 4.8 μm, which could be unambiguously attributed to deuterated PAHs in only six of the observed sources, all of which are located in the Milky Way. In all cases, the aromatic C-D stretching feature is weaker than the aliphatic C-D stretching feature, and, in the case of M17b, this feature is not observed at all. Based on the weak or absent PAD features in most of the observed spectra, it is suggested that the mechanism for PAH deuteration in the ISM is uncommon.

K.D. Doney, A. Candian, T. Mori, T. Onaka, and A.G.G.M.. Tielens, *Deuterated polycyclic aromatic hydrocarbons: Revisited*, Astronomy & Astrophysics, 586 (2016) A65

8.1 INTRODUCTION

All deuterium (D; heavy hydrogen) was formed during the Big Bang and has subsequently been depleted through the process of astration, *i.e.*, destruction by nuclear reactions in the interior of stars (Epstein et al., 1976; Linsky et al., 2006). As a result, the amount of deuterium in a galaxy, either as a free atom in the gas phase or locked up in molecules or grains, provides a direct measure of cosmic nucleosynthesis and is related to the chemical evolution of the galaxy itself. Of particular interest is the incorporation of deuterium in polycyclic aromatic hydrocarbon (PAH) molecules. These molecules are ubiquitous and abundant in the interstellar medium (ISM); their UV/visible-pumped fluorescence is almost universally believed to give rise to aromatic infrared bands (AIBs). These bands dominate the mid-infrared (MIR) spectra of many interstellar objects, such as HII regions, planetary, and reflection nebulae, the diffuse ISM, and even entire galaxies (Leger & Puget, 1984; Allamandola et al., 1985, 1989; Tielens, 2008; Joblin & Tielens, 2011; Li & Draine, 2012). The large heat capacity associated with aromaticity (Schutte et al., 1993) suggests that once formed in stellar ejecta (Frenklach & Feigelson, 1989; Cherchneff et al., 1992) the PAH molecule is stable against photodissociation, at least compared to other ISM molecules. However, studies of meteorites (Kerridge et al., 1987) and recent laboratory experiments (Sandford et al., 2000; Thrower et al., 2012; Klærke et al., 2013) show that PAHs can undergo processing, such as oxidation, reduction, and isotope exchange, which depend on the environments the PAH experience. The large size ($>$ 50 C atoms) and numerous hydrogen atoms of interstellar PAHs allows them to potentially be a large reservoir of deuterium in the ISM (Allamandola et al., 1989; Tielens, 1992; Hudgins et al., 2004). Consequently, deuterium-enriched PAHs have been suggested as a possible explanation for the variation of the gas phase atomic D/H ratio in the intermediate region of the Milky Way galaxy, which has an average value of ~14 ppm, but has a range of a factor of 4 - 5 with measurements as low as about 5.0 ppm (θ Car) and as high as about 21.8 ppm (γ^2 Vel); the 17 ppm depletion in some regions cannot be explained through astration alone (Peeters et al., 2004; Draine, 2004; Linsky et al., 2006; Onaka et al., 2014).

Deuterium atoms can replace hydrogen atom in PAHs and can participate in the same characteristic vibrational modes (Bauschlicher Jr. et al., 1997). The heavier mass of deuterium shifts the C-D vibrational modes to longer wavelengths relative to the corresponding C-H vibrational modes (Bauschlicher Jr. et al., 1997; Allamandola, 1993; Sandford et al., 2000; Hudgins et al., 2004). Hydrogen or deuterium when bonded to the carbon skeleton such that the carbon retains its sp^2 hybridization (denoted PAH or PAD, respectively) results in the aromatic C-H stretch mode at 3.29 μm (Allamandola et al., 1989; Sandford et al., 2013) or the aromatic C-D stretch mode at 4.40 μm (Bauschlicher Jr. et al., 1997; Hudgins et al., 2004). If the hydrogen or deuterium adds to the PAH, resulting in a carbon with sp^3 hybridization (denoted H_n-PAH or D_n-PAH, respectively), then the CH_2 or CDH groups show both asymmetric and symmetric aliphatic stretching modes. These features fall at 3.40 and 3.50 μm for the C-H asymmetric and symmetric stretching modes, respectively (Sandford et al., 2013), and 4.63 and 4.75 μm for the C-D asymmetric and symmetric stretching modes (Hudgins et al., 2004). Recently, Buragohain et al. (2015) showed that the 4.75 μm feature may also be due to the C-D stretch of deuteronated PAH cations (D_n-PAH^+). For both C-H and C-D aliphatic stretching modes, the intensity of the asymmetric stretch is intrinsically greater than the symmetric stretch because of the larger dipole moment. Other infrared features indicative of deuterated PAHs can arise in the 9 - 18 μm as a result of bending of the C-D bonds. However, their exact position will vary across that region depending on the number of nonadjacent D atoms (Peeters et al., 2004), in some cases superimposing on the C-H bending modes of standard PAHs.

Detection of PAD/D_n-PAHs features in the IR spectrum present the astronomer with several challenges. All three of the deuterated C-H features are predicted to be weak (Bauschlicher Jr. et al., 1997; Hudgins et al., 2004). Also, their expected positions coincide with HI emission lines, and the symmetric stretching feature at 4.75 μm is the only feature to lie in a portion of the spectrum clear

of other emission lines. Additionally, ground-based observations of deuterated PAHs are almost impeded by the absorption band of telluric CO_2 between 4.3 - 4.7 μm (Bauschlicher Jr. et al., 1997; Hudgins et al., 2004). The best targets for the search of deuterated PAHs are regions where the PAH emission is strongest, such as the surface layers of photodissociation regions (PDRs) in HII regions.

So far, deuterated PAHs have been detected by ISO-SWS in the Orion Bar and M17 primarily through the C-D asymmetric stretching feature. The estimated number of deuterium atoms relative to hydrogen atoms on PAHs (denoted PAH D/H), based on the ratio of sum of the 4.4 and 4.63 μm intensities to the 3.29 and 3.4 - 3.5 μm intensities, were found to be 0.17 ± 0.03 in the Orion Bar, and 0.36 ± 0.08 in M17 (Peeters et al., 2004) without considering the intrinsic intensities between the C-D and C-H stretching features, a factor of ~1.75 (Bauschlicher Jr. et al., 1997). The PAH D/H ratio, based on deuterated PAH features in M17, was indeed consistent with the observed Galactic variation of atomic D/H ratio in the gas phase. Recently, Onaka et al. (2014) reported an upper limit PAH D/H ratio of 0.029 ± 0.002 in the Orion Bar and 0.023 ± 0.004 in M17 with AKARI observations at slightly different pointing positions compared to the ISO-SWS observations, and taking the intrinsic intensities into account. The significant difference in the observed deuterium abundance in PAHs made it desirable to obtain multiple spectra of a large number of sources, at a variety of galactic evolution stages, with high signal-to-noise ratios to better constrain the deuterium abundance in PAHs, and to determine if the deuterium fractionation of PAHs could be not only highly variable between sources, but also within a source. To this end, we present our search for deuterated PAHs in a sample of HII regions observed with AKARI.

8.2 OBSERVATIONS AND DATA REDUCTION

The infrared camera (IRC) of the AKARI satellite offers NIR spectroscopy of the 2.5 - 5 μm region with a resolution of R ~100 for diffuse sources (Onaka et al., 2007). The observations in this study were taken during the post-helium mission phase (Phase 3) of the AKARI satellite with the Nh slit (1' × 3") with grism disperser, providing a dispersion of 0.0097 μm/px in this range (Onaka et al., 2007). At 5 μm the grism sensitivity decreases compared to 3 μm region, resulting in a larger noise level in the region where the PAD features are expected.

This study is based on the DABUN observational program, which observed seven HII regions in the Large Magellanic Cloud (LMC), five in the Small Magellanic Cloud (SMC), and eight in the Milky Way (MW), chosen based on their corresponding radio data (Paladini et al., 2003; Filipovic et al., 1998). Thirty-three additional Milky Way sources were added from the AKARI Near-Infrared Spectral Atlas of Galactic HII Regions Version 1 public release (Mori et al., 2014). The details of the observation data are given in Table 8.1.

The data reduction was carried out with the official AKARI spectroscopy pipeline for the Phase 3 data (version 20111121; Onaka et al. 2009). Spectra were extracted from the area corresponding to the brightest PAH flux at 3.3 μm. This corresponds to extraction areas of 10".22 × 3" for LMC and SMC sources, 7".3 × 3" or 10".22 × 3" for MW sources that were part of the DABUN program and 8".76 × 3" for MW sources retrieved from the AKARI public release catalog of Mori et al. (2014). The resulting spectra were subsequently spatially and spectrally smoothed by 3 pixels to remove shot noise without significantly changing the spatial or spectral resolution. In later observations, the thermal noise was noticeable even after pipeline processing, requiring additional post-pipeline dark current subtraction, which was performed following the procedure outlined by Mori et al. (2014).

For most of the targets, we took two or three observations (Table 8.1). The pointing accuracy of AKARI can vary up to about 30" between the intended and actual target pointing positions; as such we analyzed each observation separately. In the cases with three observations of the same source, the spectrum with significantly different features was removed from analysis based on the assumption that, because of limited pointing accuracy, that spectrum was observing a significantly

different part of the HII region. The selection was further reduced by removing the spectra without sufficient signal-to-noise to quantify extinction or PAH emission features.

8.3 RESULTS AND ANALYSIS

All of the analyzed spectra show a number of features, typical of HII regions, such as HI recombination lines, CO_2 ice features, and the PAH bands at 3.29 and 3.4 - 3.6 μm (Figure 8.1). The uncertainty in the relative flux calibration is less than 10%. The MW sources have better signal-to-noise compared to the LMC and SMC sources, which lie on average at distances of ∼50 kpc (Pietrzyński et al., 2013) and ∼60 kpc (Hilditch et al., 2005), respectively. As a result, while the PAH aromatic C-H stretching mode at 3.29 μm is seen in all of the spectra, in some of the LMC and SMC spectra the PAH flux is too weak to distinguish the aliphatic C-H features from the noise.

Some of the MW source spectra show ice absorption features of H_2O and CO_2, which likely arise from cold interstellar clouds between the source and AKARI. All of the obtained spectra show emission features indicative of ionized gas in HII regions. For example, the prominent HI recombination lines Brα at 4.052 μm and Brβ at 2.626 μm are seen in all spectra, and a few also show a number of other hydrogen and helium recombination lines, all of which are fit with Gaussian functions; the fit parameters are listed in Table 8.2. There is a shift in the observed central wavelength of the HI lines relative to their literature values, but the discrepancy is within the uncertainty of the wavelength calibration of ∼0.005 μm.

The continuum is fit with a third order polynomial, taking into account the broad continuum plateau from 3.2 - 3.6 μm, and then subtracted. The H_2O absorption feature around 3.05 μm is fit via laboratory spectrum of pure H_2O ice at 10 K taken from the Leiden Ice Database (Gerakines et al., 1996). In contrast, the CO_2 ice feature cannot be completely resolved using the AKARI/IRC slit spectroscopy, and is fit using a negative Gaussian function; details of the fit for the spectra are listed in Table 8.2.

The PAH and D_n-PAH fluxes at 3.29 and 4.63 μm, respectively, overlap with the HI emission lines Pfδ at 3.297 μm, Pfβ at 4.654 μm, and Huϵ at 4.673 μm. The expected HI emission intensities are determined relative to Brα and Brβ, assuming case B recombination conditions of $T_e = 10^4$ K and $n_e = 10^4$ cm^{-3} for the Milky Way and $T_e = 10^4$ K and $n_e = 10^2$ cm^{-3} for the LMC and SMC (Storey & Hummer, 1995) and an extinction law of $A_\lambda = \lambda^{-1.7}$ (Martín-Hernández et al., 2002a). To determine the flux of the underlying features, the overlapping HI lines are modeled as Gaussian functions and subtracted from the spectrum. The extinction-corrected intensity subtraction introduces an uncertainty of ∼10% to the flux of the underlying feature. The observed flux at 4.17 and 4.37 μm can be fit by the HI Hu13 and Hu12 expected flux, with some excess flux at 4.4 μm.

The PAH and H_n-PAH features and their deuterium counterparts are fit with Gaussian functions; the details of the fits are given in Table 8.2. Based on band position coincidence between observed excess flux and laboratory (Sandford et al., 2000) and theoretical data (Hudgins et al., 2004), PAD and/or D_n-PAH features were detected in six Milky Way sources: IRAS12073-6233, NGC3603, M8, M17b, W51, and G75.783+0.343 (Figures 8.1 and 8.2); the calculated PAH and H_n-PAH fluxes are summarized in Table 8.3, while the calculated PAD and D_n-PAH fluxes are summarized in Table 8.4. Of the six sources, IRAS12073-6233 and W51 had two observations that showed PAD and D_n-PAH features. In addition three sources: IRAS 15384-5348, M17a, and NGC3576, show a less than 3 σ detection of the asymmetric C-D stretch, but because of noisy baseline the accompanying symmetric mode was not seen. Aromatic C-H stretch overtone and combination bands, as well as, contributions from aliphatic side groups also fall in the range of 3.4 - 3.6 μm (Allamandola et al., 1989; Sandford et al., 2013; Pilleri et al., 2015), and similarly, contributions from the C-D analogs likely fall between 4.6 - 5.0 μm. For analysis, we assume that aliphatic groups are attached to the main PAH rings, *i.e.*, superhydrogenated PAHs/PADs contribute the majority of the flux in these wavelength ranges, and the determined strength of these bands are consequently upper limits.

The aromatic C-D stretch feature at 4.4 μm and aliphatic C-D (a)symmetric stretch features at

Table 8.1: Observation log and target parameters (in degrees)

Target	Slit center position		Observation ID	Observation date
	RA	Dec		
LMCN4A	73.029	-66.921	4300021.1, 4300021.2, 4301021.1	2008 Dec 4, 2008 Dec 4, 2009 Dec 4
LMCN83B	73.609	-69.184	4300022.1, 4300022.2, 4301022.1	2008 Nov 14, 2008 Nov 14, 2009 Nov 18
LMCN57A	83.104	-67.698	4300023.1, 4300023.2, 4301023.2	2008 Nov 8, 2008 Nov 8, 2009 Nov 8
LMCN105A-IRS1	77.453	-68.879	4300024.1, 4300024.2, 4301024.2	2008 Nov 11, 2008 Nov 11, 2009 Nov 12
LMCN91A	74.313	-68.442	4300025.1, 4300025.2, 4301025.3	2008 Nov 19, 2008 Nov 20, 2009 Nov 24
LMCN77A	72.363	-69.202	4300026.1, 4300026.2, 4301026.3	2008 Nov 16, 2008 Nov 16, 2009 Nov 18
LMCN191A	76.157	-70.908	4300027.1, 4300027.2, 4301027.4	2008 Oct 28, 2008 Oct 28, 2009 Nov 6
SMCN26	12.036	-73.249	4300028.1, 4300028.2	2008 Nov 1, 2008 Nov 2
SMCN10	11.235	-73.170	4300029.1, 4300029.2	2008 Oct 31, 2008 Nov 1
SMCN88A	21.033	-73.151	4300030.1, 4300030.2	2008 Nov 4, 2008 Nov 4
SMCN66	14.772	-72.177	4300031.1, 4300031.2, 4301031.1	2008 Nov 4, 2008 Nov 5, 2009 Nov 6
SMCN81	17.304	-73.194	4300032.1, 4300032.2	2008 Nov 3, 2008 Nov 3
IRAS14567-5846	225.230	-58.981	4300033.1, 4300033.2	2009 Feb 19, 2009, Feb 19
IRAS15384-5348	235.569	-53.976	4300034.1, 4300034.2	2009 Feb 24, 2009 Feb 24
IRAS15502-5302	238.527	-53.194	4300035.1, 4300035.2	2009 Feb 26, 2009 Feb 26
IRAS12073-6233	182.494	-62.832	4300036.1, 4300036.2	2009 Jan 28, 2009 Jan 28
GAL314.2+00.3	216.237	-60.511	4300037.1, 4300037.2	2009 Feb 14, 2009 Aug 19
GAL319.9+00.8	225.905	-57.650	4300038.1, 4300038.2	2009 Feb 19, 2009, Feb 19
GAL336.0+00.1	247.744	-48.164	4300039.1, 4300039.2	2009 Mar 3, 2009 Mar 3
GAL334.7-00.7	247.269	-49.656	4300040.1, 4300040.2	2009 Mar 3, 2009 Mar 4
M8	270.922	-24.377	5200161.1	2008 Sep 23
G8.137+0.228	270.759	-21.800	5200163.1	2008 Sep 22
W31a	272.363	-20.322	5200165.1	2008 Sep 24
W31b	272.255	-20.084	5200167.1	2008 Sep 24
M17b	275.119	-16.204	5200171.1	2008 Sep 28
M17a	275.110	-16.181	5200169.1	2008 Sep 27
W42	279.564	-6.795	5200294.1, 5200294.2	2008 Oct 2, 2008 Oct 2
G29.944-0.042	281.518	-2.653	5200295.1, 5200295.2	2008 Oct 4, 2008 Oct 4
W49A	287.568	9.108	5200299.1, 5200299.2	2008 Oct 12, 2007 Oct 13
G48.596+0.042	290.127	13.930	5200300.1, 5200300.2	2008 Oct 17, 2008 Oct 17
W51	290.561	14.051	5200301.1, 5200301.2	2008 Oct 17, 2008 oct 18
W58A	300.440	33.548	5201198.1, 5200767.1	2009 May 2, 2009 Nov 6
G70.293+1.600	300.440	33.548	5200337.1	2008 Nov 6
G75.783+0.343	305.422	37.430	5200772.1	2009 May 11
G76.383-0.621	306.863	37.381	5200343.1	2008 Nov 15
G78.438+2.659	304.913	40.943	5200776.1	2009 May 13
DR7	307.037	40.875	5200769.1	2009 May 17
G81.679+0.537	309.752	42.331	5200347.1	2008 Nov 22
G111.282-0.663	349.020	60.038	5200432.1	2009 Jan 16
RCW42	141.106	-51.990	5200452.1	2008 Dec 15
G282.023-1.180	151.653	-57.204	5200436.1	2009 Jan 1
RCW49	156.034	-57.788	5200438.1	2009 Jan 4
NGC3372	160.883	-59.580	5200440.1	2009 Jan 10
G289.066-0.357	164.124	-60.098	5200442.1	2009 Jan 13
NGC3576	167.984	-61.313	5200444.1	2009 Jan 17
NGC3603	168.756	-61.263	5200446.1	2009 Jan 17
G319.158-0.398	225.816	-59.074	5200933.1	2009 Aug 25
G330.868-0.365	242.601	-52.099	5200109.1	2008 Sep 2
G331.386-0.359	243.183	-51.748	5200113.1	2008 Sep 3
G333.122-0.446	245.255	-50.585	5200121.1	2008 Sep 4
G338.398+0.164	250.032	-46.385	5200942.1, 5200942.2	2009 Sep 7, 2009 Sep 7
G338.400-0.201	250.468	-46.582	5200943.2	2009 Sep 7
G345.528-0.051	256.538	-40.962	5200133.1	2008 Sep 11

Table 8.2: Gaussian profile parameters for ice absorption features and emission lines fitted in the spectra

Line	λ_{center} (μm)	FWHM (μm)
HI Brβ	2.6259	0.026
HI Pf13	2.6751	0.026
HI Pf12	2.7583	0.026
HI Pfη	2.8730	0.026
HI Pfϵ	3.0392	0.026
PAH	3.29	0.060
HI Pfδ	3.2970	0.026
H_n-PAH	3.40	0.058
H_n-PAH	3.45	0.058
H_n-PAH	3.50	0.058
H_n-PAH	3.56	0.058
HI Pfγ	3.7406	0.026
H_2 0-0 S(13)	3.846	0.026
HI Brα	4.0523	0.026
HI Hu13	4.1708	0.026
CO_2	4.26	0.047
He I ($^3S_1$-$^3P_0$)	4.2954	0.026
HI Hu12	4.3765	0.026
PAD	4.40	0.047
D_n-PAH	4.63	0.047
HI Pfβ	4.6538	0.026
HI Huϵ	4.6725	0.026
D_n-PAH	4.75	0.047
D_n-PAH	4.80	0.047
D_n-PAH	4.85	0.047

4.63 - 4.85 μm are present in all eight of the spectra (Figures 8.1 and 8.2), with the exception of M17b. As noted by Peeters et al. (2004) for M17, the nearby source M17b does not show the aromatic C-D stretch band. The aromatic C-D stretch mode is observed to be blended with the HI Hu12 emission line. Nonetheless, two Gaussian profiles are needed to reproduce the observed spectrum, and detections of the same blended feature in multiple sources suggest that the feature is not noise even though they are only ∼1 σ level detections. The aliphatic C-D asymmetric stretch feature is heavily blended with HI emission lines and, as a result, its intensity is an estimation based on the intrinsic intensity ratio of the C-D symmetric to asymmetric modes and the intensity of the unobscured C-D symmetric feature. Simultaneous fitting of the Pfβ, Huϵ, and estimated C-D asymmetric stretch features is able to reproduce the observed spectrum, which suggests that the estimation is good. In the case of IRAS12073-6233 and NGC3603 (Figure 8.1 a), b), c) and Figure 8.2 a), b), c)), the PAD and D_n-PAH signal to noise was large enough that the minor features seen in the Hudgins et al. (2004) modeled spectra at 4.8 - 4.9 μm are discernible. In NGC3603, however, the minor feature at 4.84 μm has a significantly larger intensity than expected based on the model in Hudgins et al. (2004), which is likely a result of the continuum subtraction.

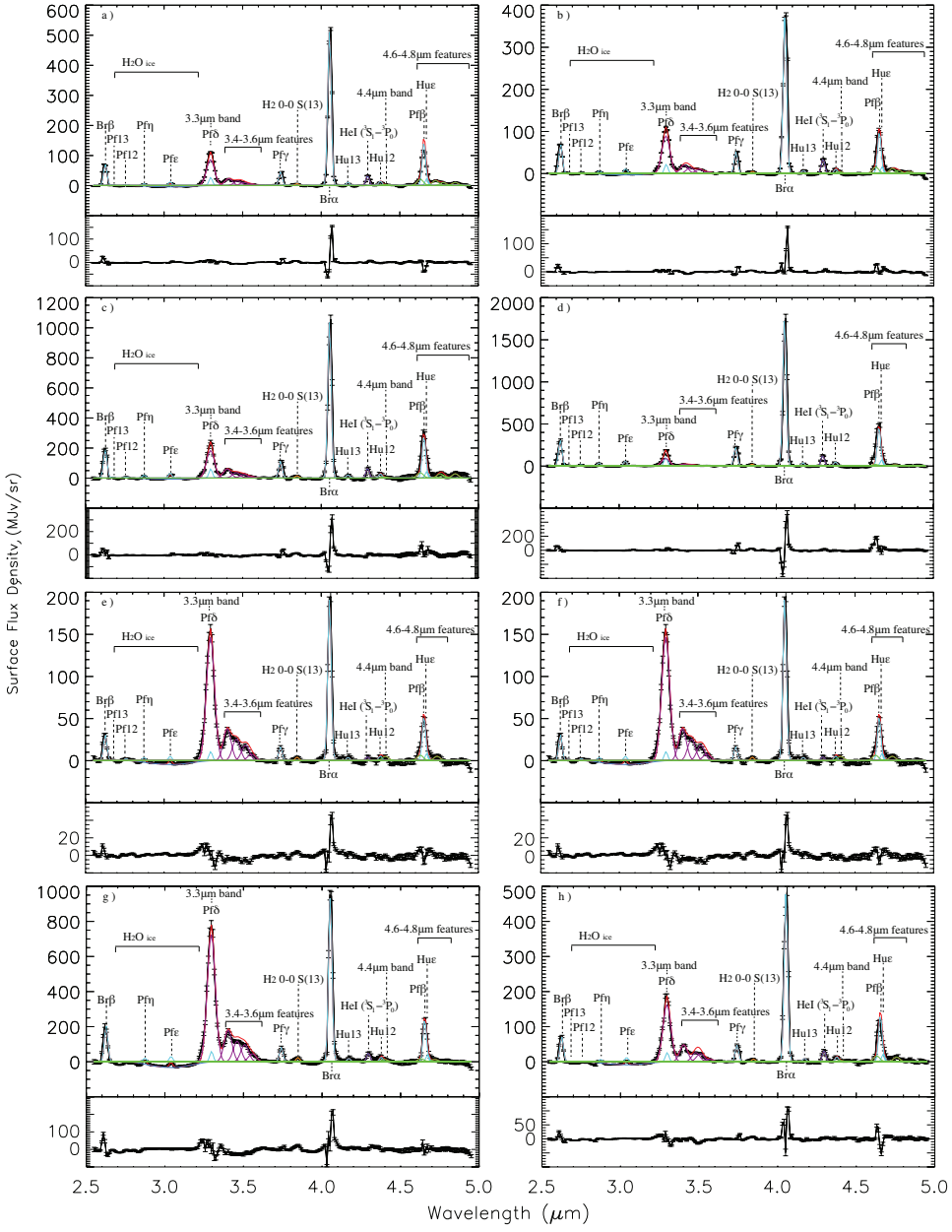

Figure 8.1: Fitting results for the spectra of a) IRAS12073-6233 obs. 1, b) IRAS12073-6233 obs. 2, c) NGC3603, d) M17b, e) W51 obs. 1, f) W51 obs. 2, g) M8, and h) G75.783+0.343 in red. The black line is the observed spectra, the HI emission lines are fit in cyan, the HeI emission line is fit in navy, the H_2O ice absorption line is fit in blue, the H_2 rotational line is fit in orange, PAH and H_n-PAH features are fit in purple, and PAD and D_n-PAH features are fit in green. Below each figure is the corresponding residual plot.

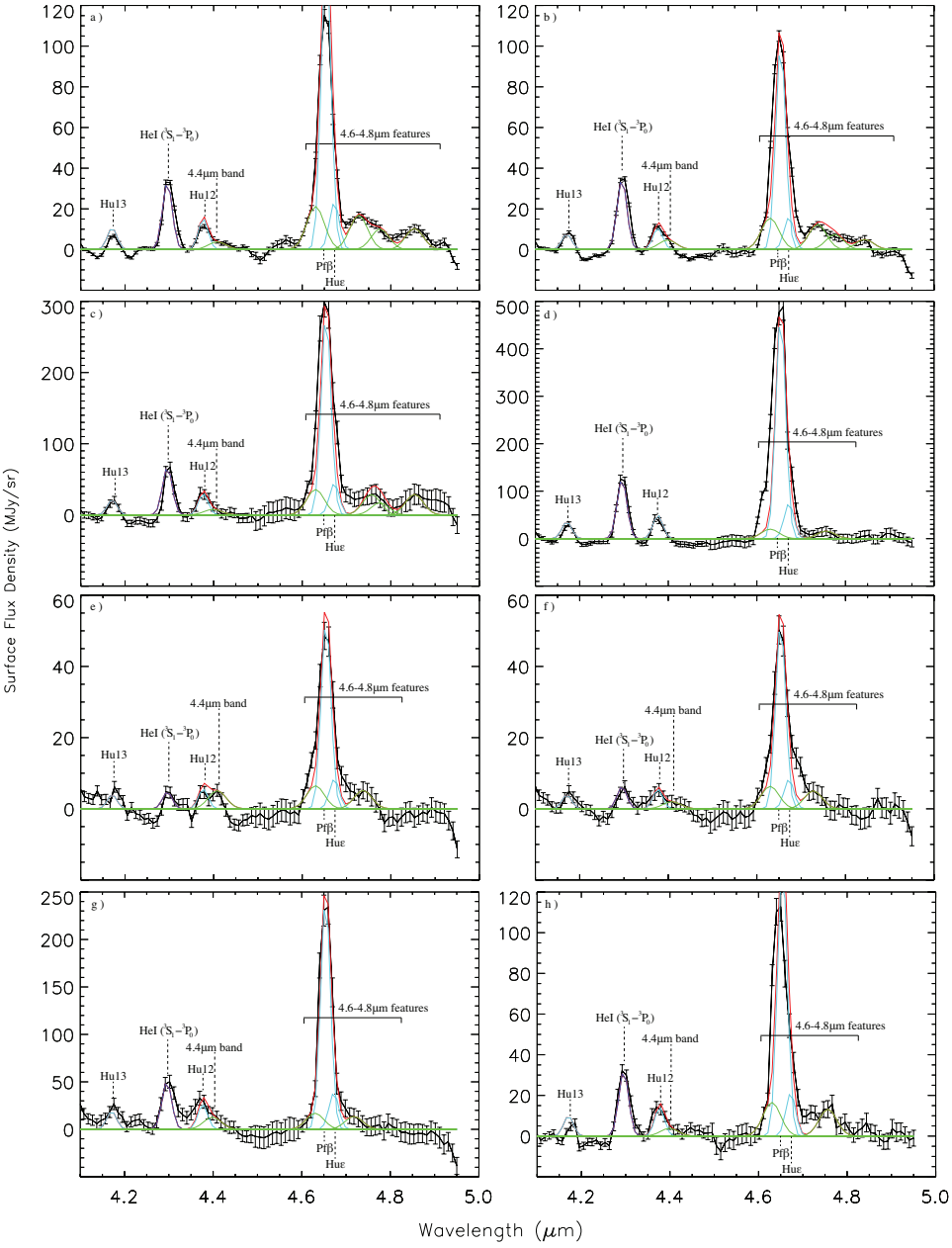

Figure 8.2: Close up of the C-D stretching region of the spectra of a) IRAS12073-6233 obs. 1, b) IRAS12073-6233 obs. 2, c) NGC3603, d) M17b, e) W51 obs. 1, f) W51 obs. 2, g) M8, and h) G75.783+0.343. The fitting results for the spectra is shown in red, the black line is the observed spectra, the HI emission lines are fit in cyan, the HeI emission line is fit in navy, and PAD and D_n-PAH features are fit in green.

Table 8.3: PAH/H_n-PAH fluxes[a] for sources with detectable deuterated features

Source	Av (mag)	3.29μm Aromatic C-H	3.4μm Asymmetric Aliphatic C-H	3.45μm[b]	3.5μm Symmetric Aliphatic C-H	3.56μm[b]
G75.783+0.343	28	22.2 ± 2.0	6.2 ± 0.6	3.3 ± 0.4	2.9 ± 0.9	0.9 ± 0.2
		125 σ	37 σ	20 σ	18 σ	5.5 σ
NGC3603	22	25.1 ± 2.4	7.8 ± 0.8	4.6 ± 0.6	3.1 ± 1.2	1.2 ± 0.5
		69 σ	23 σ	14 σ	9.5 σ	3.7 σ
W51 obs. 1	26	20.0 ± 1.8	4.8 ± 0.5	3.2 ± 0.3	2.3 ± 0.5	0.9 ± 0.2
		182 σ	47 σ	32 σ	23 σ	9.5 σ
W51 obs. 2	26	20.6 ± 1.8	4.9 ± 0.5	3.2 ± 0.3	2.2 ± 0.4	1.2 ± 0.2
		232 σ	59 σ	39 σ	27 σ	15 σ
M17b	23	12.3 ± 1.5	2.9 ± 0.5	2.1 ± 0.4	0.8 ± 0.5	0.8 ± 0.4
		20 σ	5.1 σ	3.6 σ	1.5 σ	1.4 σ
M8	16	99.1 ± 8.9	22.9 ± 2.2	14.7 ± 1.5	12.1 ± 2.2	5.5 ± 0.9
		175 σ	44 σ	28 σ	24 σ	11 σ
IRAS12073-6233 obs. 1	31	11.7 ± 1.0	2.9 ± 0.3	1.9 ± 0.2	1.3 ± 0.2	0.6 ± 0.1
		149 σ	40 σ	27 σ	18 σ	9.0 σ
IRAS12073-6233 obs. 2	22	12.2 ± 1.0	2.6 ± 0.2	1.7 ± 0.2	1.3 ± 0.2	0.5 ± 0.1
		69 σ	16 σ	11 σ	8.0 σ	2.8 σ

a. In units of 10^{-17} Wm^{-2} $arcsec^{-2}$

b. See text for discussion of the origin of these features.

Table 8.4: PAD/D_n-PAH fluxes[a] for sources with detectable deuterated features

Source	4.4μm Aromatic C-D	4.63μm Asymmetric Aliphatic C-D	4.75μm Symmetric Aliphatic C-D	4.8μm[b]	4.85μm[b]	D/H
G75.783+0.343	0.30 ± 0.19	1.26 ± 0.53	0.99 ± 0.33			0.13 ± 0.03
	1.2 σ	5.3 σ	4.2 σ			
NGC3603	0.62 ± 0.52	2.73 ± 1.57	2.13 ± 0.98	1.73 ± 0.79	2.11 ± 1.07	0.37 ± 0.10
	1.3 σ	5.8 σ	4.7 σ	3.8 σ	4.7 σ	
W51 obs. 1	0.41 ± 0.14	0.49 ± 0.29	0.39 ± 0.18			0.07 ± 0.02
	5.4 σ	6.8 σ	5.5 σ			
W51 obs. 2	0.16 ± 0.14	0.48 ± 0.29	0.38 ± 0.18			0.06 ± 0.02
	2.1 σ	6.6 σ	5.3 σ			
M17b		1.53 ± 1.19	1.19 ± 0.75			0.25 ± 0.13
		6.6 σ	5.3 σ			
M8	1.03 ± 0.53	1.05 ± 1.00	0.82 ± 0.63			0.03 ± 0.01
	4.5 σ	4.8 σ	3.8 σ			
IRAS12073-6233 obs. 1	0.30 ± 0.08	1.62 ± 0.28	1.26 ± 0.17	0.76 ± 0.15	0.76 ± 0.16	0.44 ± 0.05
	1.2 σ	6.7 σ	5.3 σ	3.2 σ	3.3 σ	
IRAS12073-6233 obs. 2	0.37 ± 0.08	1.18 ± 0.23	0.92 ± 0.23	0.46 ± 0.16	0.36 ± 0.14	0.31 ± 0.04
	3.2 σ	10.7 σ	8.5 σ	4.3 σ	3.4 σ	

a. In units of 10^{-17} Wm^{-2} $arcsec^{-2}$

b. See text for discussion of the origin of these features.

In the 3.8 - 4.6 μm region, there are a number of features that can be attributed to either HI lines, the 0 - 0 S(13) - S(9) ro-vibrational transitions of H_2, or deuterated PAHs. Notably, the S(10) transition of H_2 at 4.4 μm overlaps the expected position of the aromatic C-D stretch mode. The S(13) transition at 3.85 μm is seen clearly in all eight of the spectra. Based on the intensities of the excess flux at the positions corresponding to the S(12) - S(9) transitions of H_2 and level populations predicted by non-LTE models of H_2 (Bertoldi et al., 2000), we cannot rule out the S(10) transition of H_2 as the carrier of the 4.4 μm excess flux at the present spectral resolution. However, for the analysis we assume the 4.4 μm feature is the aromatic C-D stretch in order to obtain an upper limit on its abundance. In the case of the C-D aliphatic stretch features, the excess fluxes at 4.63 μm, and 4.75 μm do not match the S(9) transition of H_2 within the wavelength calibration uncertainties, and thus the H_2 transition does not influence their assignments.

If we only take the intrinsic intensity ratio of C-D to C-H features into account, which reduces the overall intensities for deuterium features by a factor of ~1.75 (Bauschlicher Jr. et al., 1997), the number of deuterium atoms relative to hydrogen atoms on PAHs is then estimated from the ratio of the sum of the corrected deuterated features to the sum of the hydrogenated features. An observed upper limit of the PAH D/H is determined to be between 0.03 and 0.44, which is summarized in Table 8.4. [1] For sources with multiple observations, W51 and IRAS12073-6233, it was found that the PAH D/H ratio is consistent within flux uncertainties in W51, but not in IRAS12073-6233. This may hint that very local conditions are indeed important to the deuterium variations, but more observations at higher spatial resolution are needed to confirm this.

The amount of deuterium at either an aromatic or aliphatic position was also determined through a comparison of observed PAH D/H ratios to those expected if one hydrogen is replaced with a deuterium at either an aromatic or aliphatic position. From the 3.4/3.29 μm ratio, the amount of aliphatic hydrogen relative to aromatic hydrogen, $N_{aliphatic,H}/N_{aromatic,H}$, of the PAHs in the eight observations was determined to be between 0.2 - 0.3 (Table 8.3), which is significantly larger than the $N_{aliphatic,H}/N_{aromatic,H}$ ~0.02 typically seen in PAHs in the ISM (Tielens, 2008). Additionally, neutral, small ($N_C < 50$) PAHs molecules are considered to mainly contribute to the 3.3 μm feature, so from the PAH IR Spectral Database (Boersma et al., 2014) six representative PAHs (three extended and three compact) were chosen to determine the expected D/H ratios: $C_{40}H_{22}$, $C_{40}H_{16}$, $C_{32}H_{18}$, $C_{32}H_{14}$, $C_{24}H_{14}$, and $C_{24}H_{12}$. For example, for $C_{40}H_{22}$ to get an $N_{aliphatic,H}/N_{aromatic,H}$ ~0.22, there would be four aliphatic hydrogens and 18 aromatic hydrogens. Replacement of an aromatic hydrogen with an aromatic deuterium would result in an aromatic D/H of 0.06, and replacement of one aliphatic hydrogen for an aliphatic deuterium would result in an aliphatic D/H ratio of 0.33. If this is evaluated for the six representative molecules, on average a monodeuterated D_n-PAH would have an expected aliphatic D/H of ~0.5, while a monodeuteratued PAD would have an average expected aromatic D/H of ~0.09.

The ratio of the 4.40 μm features to the 3.29 μm features gives a fractional abundance of aromatic deuterium to aromatic hydrogen of < 0.05 for all eight observations. In contrast, based on the sum of the 4.63 and 4.75 μm features relative to the sum of the 3.40 and 3.50 μm features, the fractional abundance of aliphatic deuterium relative to aliphatic hydrogen is much larger, varying from 0.09 to 1. For a representative PAH, for example, the hydrogenated PAH $C_{40}H_{18}$, these observed deuterium abundances would yield at most 1 aromatic deuterium, 2 aliphatic deuterium, 13 aromatic hydrogen, and 2 aliphatic hydrogen, and a PAH D/H of 0.2, which is roughly representative of the average of the values determined for the eight observations. Based on the expected D/H ratios, it is estimated that in all eight observations less than 10% of the observed PAHs have one aromatic deuterium. Conversely, with the exception of the PAHs in W51 and M8, all of the observed PAHs have at least one aliphatic deuterium. In particular, the aliphatic D/H ratios for IRAS12073-6233

1 The PAH D/H is calculated as the sum of the deuterium feature fluxes (Table 8.4 columns 2 - 6) divided by a factor of 1.75 to account for intrinsic intensities, divided by the sum of the hydrogen feature fluxes (Table 8.3 columns 3 - 7). The given PAH D/H uncertainties in Table 8.4 do not take errors of various origins into account, including the difference of excitation of PADs/D_n-PAHs and PAHs/H_n-PAHs, the assignment uncertainties of minor spectral features, or the uncertainties in the intrinsic intensities between different vibrational modes.

and M17b are more in agreement with the PAHs having one aliphatic deuterium for every aliphatic hydrogen. Furthermore, the aliphatic D/H ratios ~0.4 and ~0.30 for IRAS12073-6233 obs. 1 and obs. 2, respectively, suggest that almost all of the deuterium is in aliphatic positions.

The determined amount of deuterium relative to hydrogen on PAHs are upper limits, and a more complete understanding would include the effects of the emission process on the band intensities; to understand these effects we calculated the emission spectrum of a prototype PAH molecule, neutral ovalene, where one solo hydrogen is substituted with a $-CH_2D$ group (N_C = 33). To model the emission process, we follow the procedure described in Candian et al. (2012), where both the infrared spectrum of the molecule in question and its photoabsorption cross-section were evaluated with quantum chemistry techniques. As the effective temperature of the exciting source, we assume T_{eff} = 40000 K, as in IRAS 12073-6233 (Martín-Hernández et al., 2002b), which is one of the HII regions in our sample.

For this molecule, the intrinsic 3.3/4.75 μm (C-H aromatic/C-D aliphatic) ratio is 1.81 (consistent with earlier calculations of Bauschlicher Jr. et al. (1997)). The emission process brings the band ratio to 0.64, which then will correspond to a D/H range of 0.01 - 0.16 in our sample. These values are clearly sensitive to the parameters assumed in the emission model (*e.g.*, effective temperature, PAH size), for example, M17. Peeters et al. (2004) did not consider the emission process and found a D/H = 0.36 ± 0.08, while for the same source Onaka et al. (2014) via an emission model that favored larger PAHs found an upper limit D/H = 0.023 ± 0.004. Similarly, we find a D/H = 0.09 ± 0.05 for the nearby source M17b via our emission model, which favors smaller PAHs. Therefore, the observed band intensity ratio can overestimate the actual relative abundance of deuterium to hydrogen on PAHs and the amount is dependent on the emission process. Stronger constraints on the typical PAH size population and exciting source characteristics in HII regions would improve our estimate of the deuterium abundance.

8.4 DISCUSSION

High levels of deuteration have been observed in some species, *e.g.*, CD_3OH, ND_3 (Parise et al., 2004; Lis et al., 2002; van der Tak et al., 2002), which are thought to originate from grain surface chemistry (Roberts et al., 2003). Deuterium fractionation is not as extensive for PAHs. In the best case (IRAS12073-6233 observation 1), the PAH D/H value is 0.44 (Table 8.4), which would translate to a fraction of gas-phase atomic deuterium (relative to hydrogen) locked up in PAHs of roughly 18 ppm; these are determined following the analysis method outlined in Onaka et al. (2014). Of the sources with observed deuterated PAHs, the average PAH D/H fraction is 0.21, which corresponds to a locked up fraction of gas-phase deuterium (relative to hydrogen) of about 10 ppm. Observation of atomic deuterium in the local ISM shows strong variation in the D/H abundance ratio of the gas phase at the 17 ppm level (Linsky et al., 2006). While our observations are not along the same lines of sight, they indicate that PADs and D_n-PAHs would be a major reservoir of elemental deuterium. Moreover, our study also reveals strong variation in the deuterated PAH to PAH ratio. Hence, the interaction of atomic deuterium with PAHs could well be at the origin of the observed variation in the gas-phase deuterium abundance.

While deuterated PAHs are not omnipresent, when present, deuteration is efficient; all eight observations have a PAH D/H ratio that is significantly greater than the cosmic gas-phase abundance of $\sim 10^{-5}$ (Vidal-Madjar et al., 1998). Incorporation of deuterium into PAHs can occur through a number of mechanisms, most of which are driven by the small difference in zero-point energy between hydrogen and deuterium. Deuterium enrichment can take place in the gas phase or through solid state reactions within ice or on grains.

Large deuteration fractionation can occur in PDRs at depths where most of the hydrogen is locked up in H_2, but deuterium is still mainly atomic. H_2 and HD are expected to show different behavior with depth into a cloud, as self-shielding of H_2 pulls the H/H_2 transition to the surface of the PDR. Conversely, self-shielding is of little importance for HD, and photodestruction converts

HD to atomic deuterium (Tielens, 1992). Through gas-phase addition reactions, the free atomic deuterium adds aliphatically to the PAH molecule. Recent theoretical calculations (Ricca et al., 2007; Rauls & Hornekær, 2008; Rasmussen et al., 2011) and experiments (Thrower et al., 2012; Klærke et al., 2013; Demarais et al., 2014) demonstrate that hydrogenation (H_n-PAH) or deuteration (D_n-PAH) can be important through reactions in the gas phase in regions of the PDR without intense UV radiation. The addition occurs preferentially on carbons at the edges of PAH molecules and gives the carbon an aliphatic character (Rauls & Hornekær, 2008). Rasmussen et al. (2011) and Rauls & Hornekær (2008) calculated the first hydrogen addition to the periphery has a barrier of 0.06 eV for neutral PAHs, while the second hydrogen addition is barrierless. For cations, hydrogenation is even easier, since the first hydrogen addition is barrierless and the second addition has a negligible barrier (Ricca et al., 2007). Similar mechanisms can be employed to explain the presence of aliphatic deuterium on PAHs. In an evaporating flow, the PAHs move to the surface of the PDR and then into the general ISM, during which the deuterium fractionation is temporarily preserved. In this schematic way, we can understand how PAHs can be highly fractionated, that this fractionation primarily occurs as aliphatic H/D, and that this fractionation behavior is very sensitive to the local conditions and history of the PAHs. Thus, it is expected to vary from one region to the next.

Additionally, ion-molecule and neutral-neutral addition reactions occur at low temperatures, but require that the reaction is exothermic or has no barrier (Dalgarno & Lepp, 1984; Tielens, 1992; Bauschlicher Jr., 1998; Sandford et al., 2001). These reactions, in the gas phase or on grain surfaces, are proposed to lead to both aliphatic and aromatic deuterated or hydrogenated PAHs deep inside dense clouds,

$$\mathrm{PAH} + \mathrm{H_2D^+} \rightarrow \mathrm{D_n - PAH^+} + \mathrm{H_2}$$

$$\mathrm{PAH} + \mathrm{H_3^+} \rightarrow \mathrm{H_n - PAH^+} + \mathrm{H_2}$$

$$\mathrm{H_n - PAD^+} + \mathrm{e^-} \rightarrow \mathrm{PAD} + \mathrm{H}$$

$$\mathrm{D_n - PAH^+} + \mathrm{e^-} \rightarrow \mathrm{PAH} + \mathrm{D}$$

$$\mathrm{H_n - PAH^+} + \mathrm{e^-} \rightarrow \mathrm{PAH} + \mathrm{H}$$

Similar reaction schemes are responsible for the deuteration of small hydrocarbon species, such as HCO^+ and HCN. Deuteration fractionation in these species is observed to reach levels of $\sim 4 \times 10^{-2}$ (Roberts et al., 2002).

At temperatures less than 50 K, most of the volatile molecules are frozen out onto the dust grains (Boogert et al., 2015). Penetrating UV radiation from nearby O/B stars or photon-induced, cosmic-ray ionization that is deep inside dense cores has enough energy to break the molecular bonds on smaller molecules producing radicals. These highly reactive species, in turn, can go on to form new bonds (Bernstein et al., 2001; Sandford et al., 2001). Laboratory experiments of PAHs in deuterium-enriched water ices demonstrated that under UV irradiations PAHs undergo oxidation, reduction, and deuterium-hydrogen exchange reactions. Deuterium enrichment in ices is independent of the size of the PAH, and seems to favor the aromatic deuterium product (PAD) over aliphatic addition, resulting in enrichment levels of at least D/H $\sim 10^{-4}$ (Sandford et al., 2000).

Independent of the temperature, PAHs can undergo unimolecular photodissociation if they absorb a UV photon with enough energy to break the C-H bond. The aliphatic sp^3 bonds are more labile compared to the aromatic sp^2 bonds, favoring the loss of an aliphatic hydrogen or deuterium over an aromatic hydrogen or deuterium atom. The presence of aliphatic bonds also causes the PAH geometry to depart from planarity, adding stress to the molecule and resulting in weaker C-H bonds than in fully aromatic, planar PAH molecules. The lower zero-point energy of deuterium suggests that dehydrogenation is favored over dedeuteration at ISM temperatures, $T < 70$ K. In addition, since larger PAHs have larger heat capacities relative to small PAHs, unimolecular photodissociation favors PAHs with less than 50 carbon atoms. Theoretical estimates suggest that the expected deuterium fractionation from this method in HII regions is about 10^{-5} (Allamandola

et al., 1989). The low abundance or complete lack of observed deuterated features in a majority of the observed sources suggests that the conditions leading to deuterium addition in the ISM are not common. Further theoretical studies are required to assess the different scenarios in more detail.

The upcoming James Webb Space Telescope (JWST) will offer significantly better spectral resolution in the NIR, from 1 - 5 μm, which will allow for better resolution of the 4.63 and 4.75 μm features, and even better constraint on the abundance of deuterium on PAHs, in the Milky Way, and in the neighboring LMC and SMC. Additionally, JWST will offer similar resolution mid-IR spectroscopy from 5 - 28 μm, which gives access to the intrinsically stronger C-D bending modes in addition to the C-D stretch modes. Since the C-D bending features are hard to unambiguously distinguish from the C-H bending features of PAH cations, the simultaneous detection of the C-D bending and C-D stretching features is needed for a stronger confirmation that deuterated PAHs were detected; this is a unique capability of JWST, which previous telescopes, for example, the Spitzer Space Telescope, were not able to do.

8.5 ACKNOWLEDGEMENTS

K.D.D. thanks Dr. E. Peeters for useful and stimulating discussions. This research is based on observations with AKARI, a JAXA project with the participation of ESA. Studies of interstellar PAHs at Leiden Observatory are supported through advanced European Research Council grant 246976 and a Spinoza award.

8.6 BIBLIOGRAPHY

Allamandola, L. J. 1993, in Astronomical Society of the Pacific Conference Series, Vol. 41, Astronomical infrared spectroscopy: Future observational directions, ed. S. Kwok, 197

Allamandola, L. J., Tielens, A. G. G. M., & Barker, J. R. 1985, The Astrophysical Journal, 290, L25

Allamandola, L. J., Tielens, A. G. G. M., & Barker, J. R. 1989, The Astrophysical Journal Supplements, 71, 733

Bauschlicher Jr., C. W. 1998, The Astrophysical Journal, 509, L125

Bauschlicher Jr., C. W., Langhoff, S. R., Sandford, S. A., & Hudgins, D. M. 1997, The Journal of Physical Chemistry A, 101, 2414

Bernstein, M. P., Dworkin, J. P., Sandford, S. A., & Allamandola, L. J. 2001, Meteoritics and Planetary Science, 36, 351

Bertoldi, F., Draine, B. T., Rosenthal, D., et al. 2000, in IAU Symposium, Vol. 197, From Molecular Clouds to Planetary, ed. Y. C. Minh & E. F. van Dishoeck, 191

Boersma, C., Bauschlicher Jr., C. W., Ricca, A., et al. 2014, The Astrophysical Journals, 211, 8

Boogert, A., Gerakines, P., & Whittet, D. 2015, ArXiv e-prints

Buragohain, M., Pathak, A., Sarre, P., Onaka, T., & Sakon, I. 2015, Monthly Notices of the Royal Astronomical Society, 454, 193

Candian, A., Kerr, T. H., Song, I.-O., McCombie, J., & Sarre, P. J. 2012, Monthly Notices of the Royal Astronomical Society, 426, 389

Cherchneff, I., Barker, J. R., & Tielens, A. G. G. M. 1992, The Astrophysical Journal, 401, 269

Dalgarno, A. & Lepp, S. 1984, The Astrophysical Journal, 287, L47

Demarais, N. J., Yang, Z., Snow, T. P., & Bierbaum, V. M. 2014, The Astrophysical Journal, 784, 25

Draine, B. T. 2004, ArXiv Astrophysics eprint arXiv:astro-ph/0410310

Epstein, R. I., Lattimer, J. M., & Schramm, D. N. 1976, Nature, 263, 198

Filipovic, M. D., Jones, P. A., White, G. L., & Haynes, R. F. 1998, Astronomy & Astrophysicss, 130, 441

Frenklach, M. & Feigelson, E. D. 1989, The Astrophysical Journal, 341, 372

Gerakines, P. A., Schutte, W. A., & Ehrenfreund, P. 1996, Astronomy & Astrophysics, 312, 289

Hilditch, R. W., Howarth, I. D., & Harries, T. J. 2005, Monthly Notices of the Royal Astronomical Society, 357, 304

Hudgins, D. M., Bauschlicher Jr., C. W., & Sandford, S. A. 2004, The Astrophysical Journal, 614, 770

Joblin, C. & Tielens, A. G. G. M., eds. 2011, EAS Publications Series, Vol. 46, PAHs and the Universe: A symposium to celebrate the 25th anniversary of the PAH hypothesis

Kerridge, J. F., Chang, S., & Shipp, R. 1987, Geochimica Cosmochimica Acta, 51, 2527

Klærke, B., Toker, Y., Rahbek, D. B., Hornekær, L., & Andersen, L. H. 2013, Astronomy & Astrophysics, 549, A84

Leger, A. & Puget, J. L. 1984, Astronomy & Astrophysics, 137, L5

Li, A. & Draine, B. T. 2012, The Astrophysical Journal, 760, L35
Linsky, J. L., Draine, B. T., Moos, H. W., et al. 2006, The Astrophysical Journal, 647, 1106
Lis, D. C., Roueff, E., Gerin, M., et al. 2002, The Astrophysical Journal, 571, L55
Martín-Hernández, N. L., Peeters, E., Morisset, C., et al. 2002a, Astronomy & Astrophysics, 381, 606
Martín-Hernández, N. L., Vermeij, R., Tielens, A. G. G. M., van der Hulst, J. M., & Peeters, E. 2002b, Astronomy & Astrophysics, 389, 286
Mori, T. I., Onaka, T., Sakon, I., et al. 2014, The Astrophysical Journal, 784, 53
Onaka, T., Lorente, R., & Ita, Y. 2009, IRC data users's manual for Phase 3 ver 1.1
Onaka, T., Matsuhara, H., Wada, T., et al. 2007, Publications of the Astronomical Society of Japan, 59, 401
Onaka, T., Mori, T. I., Sakon, I., et al. 2014, The Astrophysical Journal, 780, 114
Paladini, R., Burigana, C., Davies, R. D., et al. 2003, Astronomy & Astrophysics, 397, 213
Parise, B., Castets, A., Herbst, E., et al. 2004, Astronomy & Astrophysics, 416, 159
Peeters, E., Allamandola, L. J., Bauschlicher Jr., C. W., et al. 2004, The Astrophysical Journal, 604, 252
Pietrzyński, G., Graczyk, D., Gieren, W., et al. 2013, Nature, 495, 76
Pilleri, P., Joblin, C., Boulanger, F., & Onaka, T. 2015, Astronomy & Astrophysics, 577, A16
Rasmussen, J. A., Henkelman, G., & Hammer, B. 2011, The Journal of Chemical Physics, 134, 164703
Rauls, E. & Hornekær, L. 2008, The Astrophysical Journal, 679, 531
Ricca, A., Bakes, E. L. O., & Bauschlicher Jr., C. W. 2007, The Astrophysical Journal, 659, 858
Roberts, H., Fuller, G. A., Millar, T. J., Hatchell, J., & Buckle, J. V. 2002, Planetary Space Science, 50, 1173
Roberts, H., Herbst, E., & Millar, T. J. 2003, The Astrophysical Journal, 591, L41
Sandford, S. A., Bernstein, M. P., Allamandola, L. J., Gillette, J. S., & Zare, R. N. 2000, The Astrophysical Journal, 538, 691
Sandford, S. A., Bernstein, M. P., & Dworkin, J. P. 2001, Meteoritics and Planetary Science, 36, 1117
Sandford, S. A., Bernstein, M. P., & Materese, C. K. 2013, The Astrophysical Journal, 205, 8
Schutte, W. A., Tielens, A. G. G. M., & Allamandola, L. J. 1993, The Astrophysical Journal, 415, 397
Storey, P. J. & Hummer, D. G. 1995, Monthly Notices of the Royal Astronomical Society, 272, 41
Thrower, J. D., Jørgensen, B., Friis, E. E., et al. 2012, The Astrophysical Journal, 752, 3
Tielens, A. G. G. M. 1992, in IAU Symposium, Vol. 150, Astrochemistry of Cosmic Phenomena, ed. P. D. Singh, 91
Tielens, A. G. G. M. 2008, Annual Review of Astronomy and Astrophysics, 46, 289
van der Tak, F. F. S., Schilke, P., Müller, H. S. P., et al. 2002, Astronomy & Astrophysics, 388, L53
Vidal-Madjar, A., Lemoine, M., Ferlet, R., et al. 1998, Astronomy & Astrophysics, 338, 694